AIAA JOURNAL
Vol. 48, No. 11, November 2010

Far-Field Analysis of the Aerodynamic Force by Lamb Vector Integrals

C. Marongiu*
Centro Italiano Ricerche Aerospaziali, 81043 Capua, Italy
and
R. Tognaccini†
Università di Napoli Federico II, 80125 Naples, Italy

DOI: 10.2514/1.J050326

A new far-field method is proposed for the analysis of the aerodynamic force acting on an airfoil in subsonic unsteady flow conditions given a numerical solution of the flowfield. For this purpose, a recent theory proposed by Wu et al. (Wu, J.-Z., Ma, H.-Y., and Zhou, M.-D., *Vorticity and Vortex Dynamics*, Springer, New York, 2006), relating the aerodynamic force acting on a body to the Lamb vector (the cross product of the vorticity by the velocity) in case of unsteady Navier–Stokes flow, has been extended to the analysis of high-Reynolds-number turbulent flows governed by the Reynolds-averaged Navier–Stokes equations. The applications showed here concern the analysis of numerical solutions around an airfoil in steady flow and in pitching oscillations including a dynamic-stall condition. Both lift and drag coefficients have been computed by means of Lamb vector integrals and have been compared with the reference near-field results (stress integration on the body). The method allows for the decomposition of the aerodynamic force in a contribution associated with the bound vorticity on the body and a contribution related to the free vorticity developing in the airfoil wake.

Nomenclature

$\underline{\mathbf{a}}$	=	fluid acceleration
C_d	=	drag coefficient
C_l	=	lift coefficient
$(C_d)_B$	=	drag coefficient contribution of the body motion
$(C_d)_\Sigma$	=	drag coefficient contribution of the Lamb surface integral
$(C_d)_\Omega$	=	drag coefficient contribution of the Lamb volume integral
$(C_d)_{\dot{\omega}}$	=	drag coefficient contribution of the vorticity time derivative
$(C_l)_B$	=	lift coefficient contribution of the body motion
$(C_l)_\Sigma$	=	lift coefficient contribution of the Lamb surface integral
$(C_l)_\Omega$	=	lift coefficient contribution of the Lamb volume integral
$(C_l)_{\dot{\omega}}$	=	lift coefficient contribution of the vorticity time derivative
c	=	airfoil chord
d	=	space dimension
$\mathrm{d}S$	=	surface element
$\mathrm{d}V$	=	volume element
$\underline{\mathbf{F}}$	=	aerodynamic force
$\underline{\mathbf{F}}_i$	=	contributions of the aerodynamic force, $i =$ I, II, III
$\underline{\mathbf{F}}_{\mathrm{I},a}$	=	advection form
$\underline{\mathbf{F}}_{\mathrm{I},d}$	=	diffusion form
$\underline{\underline{\mathbf{I}}}$	=	unit tensor
$\underline{i}$	=	x-direction versor
$\underline{j}$	=	y-direction versor
k	=	reduced frequency ($\omega c/2U_\infty$)
$\underline{k}$	=	z-direction versor
$\underline{\boldsymbol{l}}$	=	Lamb vector
$\langle \underline{\boldsymbol{l}}'' \rangle$	=	mean fluctuating Lamb vector
$\underline{n}$	=	normal versor (n_x, n_y, n_z)
p	=	pressure
$\underline{\mathbf{r}}$	=	modified position vector $[\underline{\mathbf{x}}/(d-1)]$
U_∞	=	freestream velocity
$\underline{\mathbf{u}}$	=	velocity vector (u, v, w)
x_S	=	distance of the surface Σ_I from the airfoil surface
y_S	=	distance of the surface Σ_J from the airfoil surface
α	=	angle of attack
B	=	body volume
δ	=	boundary-layer thickness
∂B	=	boundary of B
$\partial\Omega$	=	boundary of Ω
κ	=	turbulent kinetic energy
ν	=	kinematic viscosity
ν_T	=	eddy viscosity
Σ	=	external surface ($\Sigma_I \cup \Sigma_J$)
$\underline{\underline{\tau}}$	=	stress tensor
$\underline{\underline{\tau}}^t$	=	Reynolds stress tensor
$\underline{\mathbf{x}}$	=	position vector (x, y, z)
Ω	=	fluid volume
$\underline{\omega}$	=	vorticity
$\langle\cdot\rangle$	=	averaged quantities
$(\cdot)^b$	=	bound vorticity contribution
$(\cdot)^f$	=	free vorticity contribution
$(\cdot)_r$	=	reference quantities
$(\cdot)'$	=	fluctuating quantities
$(\cdot)^*$	=	normalized quantities

Received 2 November 2009; revision received 23 July 2010; accepted for publication 23 July 2010.

*Research Engineer.
†Associate Professor, Department of Aerospace Engineering. Senior Member AIAA.

I. Introduction

THE computation and measurement of the aerodynamic drag represents one of the most delicate aspects of the aircraft design. The matter is object of a significant research effort and of an intense debate in the aerospace community. The AIAA periodically plans dedicated workshops on the drag prediction of aeronautical configurations [1,2]. The goal of predicting the drag within the accuracy of one drag count ($\Delta C_d = 10^{-4}$) seems to be still far from the industrial practice, even if this uncertainty for a commercial aircraft may correspond to about two thousand pounds in terms of payload [3].

This example gives an idea of the tremendous impact that a drag variation has on the whole performance of an aircraft, and the consequences in terms of engine design, weight and consumptions.

The classical near-field methods, namely the solid surface integration of the pressure and shear stresses, and the far-field methods, derived from the integral balance of the momentum equations, are the two main categories in which all the drag calculation techniques based on the fluid dynamic field knowledge are included. Some authors [4] distinguish also the mid field methods as those obtained from the far-field after a transformation of the surface integrals into volume integrals. In any case, we can consider them as sub class of the far-field ones.

The far-field methods offer several features that make them more attractive with respect the standard near-field technique. First of all, the far-field methods can allow for an explicit interpretation of the physical processes involved in the genesis of the aerodynamic force. By means of the integral balance on a proper control volume, the breakdown of the aerodynamic coefficients is possible and the specific contributions to the total drag (induced, viscous and wave drag), are definable [5,6]. Nevertheless, by a near-field method only the mechanical breakdown of the aerodynamic force (pressure and viscous contributions) is obtainable. This feature comes out useful for the aerodynamic design and optimization processes. The theoretical research on more suitable far-field formula specialized for the induced drag is particularly significant [7] as well.

In the experimental aerodynamics, the far-field methods are widely employed because they represent an effective and non-intrusive technique to extract the drag component from a wind tunnel simulation. In the last years, a renewed interest on these aspects has been noted thanks to the growing popularity of measurement techniques such as the particle image velocimetry (PIV) [8,9].

Finally, the computational fluid dynamics (CFD) community holds a particular interest on the capabilities of the far-field methods applied to a given numerical flow solution. Even if the near-field and far-field formulations should provide the same information, on condition that the numerical solution is fully converged everywhere in the field, there is the possibility through the far-field methods to exclude spurious contributions from the aerodynamic force computation. These techniques allow to obtain a weaker grid dependency on the computed drag, so avoiding expensive convergence studies, especially on complex and three dimensional configurations [6,10,11].

Presently, the far-field methods apply to steady flows only. It does not exist a well established and tested far-field method for unsteady flow regimes. The reason of this gap is probably due to the priority that the steady state methods have had in the last decade with respect to the unsteady ones, especially in the industrial environment. However, the growing computer powers permit to deal with more complex fluid dynamic problems and a renewed interest for far-field methods in the unsteady version arises. The objective of the present paper is to meet these requirements.

The extension of the available drag prediction methods to unsteady flows does not seem straightforward. A possible alternative in this regard, can be given by the theoretical research carried out on the vortex dynamics. Several interesting theories able to supply the aerodynamic force also in the unsteady case have been developed even if for incompressible flows based on the analysis of the vorticity field.

Actually, the idea to associate the vorticity with the aerodynamic force is not new. Already Prandtl developed his lifting line theory at the beginning of the 20th century by connecting a vortex distribution to the lift generated around a finite wing. In 1935, von Karman and Burgers [12] introduced the concept of vortex force associated with an integral of the Lamb vector $\underline{\boldsymbol{l}} = \underline{\omega} \times \underline{\mathbf{u}}$, defined as the cross product of the vorticity by the velocity (see Saffman [13]).

Among various results, the paper of Wu [14] is relevant because it constitutes a first aerodynamic theory for viscous and unsteady flows with aerodynamic force expressions alternative to the near-field formulae. Wu [14] found a theoretical correlation between the aerodynamic force and the first moment of the vorticity under the hypotheses of an unbounded domain and assuming some particular asymptotic behaviors of the far-field velocities. In 1994, this result was used by Panda and Zaman [15] in a wind tunnel facility by measuring the vorticity around an oscillating airfoil at Reynolds number $4.4 \cdot 10^4$. Thus the real possibility to infer the unsteady aerodynamic force through the vorticity field was showed. A widely used method in the PIV community was developed by Noca et al. [16], who derived a far-field form only in terms of velocity and its derivatives on the surfaces of the control volume.

In 2006, Wu et al. [17] published an extension of Wu's formulation [14] in which some of its original restricting hypotheses were removed. In this theory, the Lamb vector appears to be the key quantity in the generation of the aerodynamic force. The same research group [18] showed a numerical application of this theory to flows at relatively low Reynolds number ($\sim 10^4$). Nonetheless, there are not yet published results concerning the use of such theory in flows at very high-Reynolds-number ($\geq 10^5$).

The theory presented by Wu et al. [17] provides an exact expression of the aerodynamic force for unsteady incompressible viscous flows. As will be shown in the following, it expresses the force through the sum of the volume integral of the Lamb vector (vortex force) and several surface integrals.

The aim of the present paper is to explore the potentialities of the theory of Wu et al. [17] in predicting the aerodynamic force for high-Reynolds turbulent flows. For this purpose, it has been necessary to extend the theory to allow for the analysis of flows around bodies governed by the Reynolds-averaged Navier–Stokes (RANS) equations. By means of suitable averages of the Lamb vector, we show a practical way to extract the aerodynamic force from a numerical flowfield including the possibility to deal with unsteady flow regimes.

The paper is organized as follows. In Sec. II a brief review of the theory proposed by Wu et al. [17] is reported. In Sec. III, a new formulation is proposed and discussed with an emphasis for turbulent flows. Applications to turbulent flowfields around a two dimensional airfoil in both steady and unsteady conditions are presented in Sec. IV. Comparisons of the aerodynamic force computed between the far-field technique and the classical wall integration method are shown to verify and validate the results. In Sec. V, some concluding remarks are drawn.

II. Far-Field Theory

We consider an unsteady incompressible flow around a solid body governed by the Navier–Stokes equations with uniform asymptotic conditions. The integral momentum balance straightforward provides the near-field and far-field form of the aerodynamic force $\underline{\mathbf{F}}$, exerted on the solid body B:

$$\underline{\mathbf{F}} = \underbrace{\int_{\partial B} (p\underline{\underline{\mathbf{I}}} - \underline{\underline{\tau}}) \cdot \underline{n}\, \mathrm{d}S}_{\text{Near field}} = \underbrace{-\int_{\Omega} \underline{\mathbf{a}}\, \mathrm{d}V - \int_{\Sigma} (p\underline{\underline{\mathbf{I}}} - \underline{\underline{\tau}}) \cdot \underline{n}\, \mathrm{d}S}_{\text{Far field}} \quad (1)$$

where ∂B is the closed surface of B and Σ is a closed external surface of a fixed control volume Ω (see Fig. 1). In Eq. (1), the force $\underline{\mathbf{F}}$ and the pressure p are divided by the density, $\underline{\underline{\mathbf{I}}}$ is the unit tensor, $\underline{\underline{\tau}} = \nu(\nabla \underline{\mathbf{u}} + \nabla \underline{\mathbf{u}}^T)$ is the viscous stress tensor, ν is the kinematic viscosity, $\underline{n}$ is the normal versor, positive when pointing outward, $\underline{\mathbf{u}}$ is the velocity vector and

$$\underline{\mathbf{a}} = \frac{\partial \underline{\mathbf{u}}}{\partial t} + \underline{\mathbf{u}} \cdot \nabla \underline{\mathbf{u}}$$

is the fluid acceleration.

Wu et al. [17] showed that $\underline{\mathbf{F}}$ can be expressed through the sum of three contributions:

$$\underline{\mathbf{F}} = \underline{\mathbf{F}}_{\mathrm{I}} + \underline{\mathbf{F}}_{\mathrm{II}} + \underline{\mathbf{F}}_{\mathrm{III}} \quad (2)$$

The contribution $\underline{\mathbf{F}}_{\mathrm{I}}$ is formed by a volume integral on Ω:

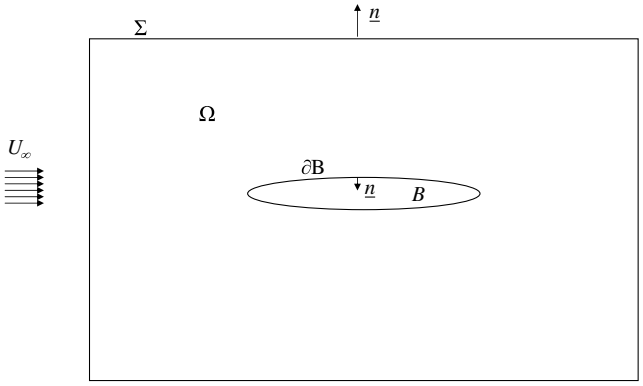

Fig. 1 Schematic representation of the control volume Ω, the body surface ∂B and external surface Σ. $\underline{n}$ is directed outward of Ω.

$$\underline{\mathbf{F}}_{\mathrm{I}} = -\int_{\Omega} (\underline{\mathbf{r}} \times \nu \nabla^2 \underline{\omega})\, \mathrm{d}V \quad \text{(diffusion form)} \tag{3}$$

In Eq. (3) $\underline{\mathbf{r}} = \underline{\mathbf{x}}/(d-1)$, $\underline{\mathbf{x}}$ is the position vector and d is the space dimension ($d = 2, 3$). Equation (3) is called diffusion form; in the following, it will be labeled with $\underline{\mathbf{F}}_{\mathrm{I},d}$. The second contribution $\underline{\mathbf{F}}_{\mathrm{II}}$ is made by surface integrals on Σ:

$$\underline{\mathbf{F}}_{\mathrm{II}} = -\int_{\Sigma} (\underline{\mathbf{r}} \times [\underline{n} \times \nu(\underline{\nabla} \times \underline{\omega})])\, \mathrm{d}S + \int_{\Sigma} \nu(\underline{\omega} \times \underline{n})\, \mathrm{d}S \tag{4}$$

Finally, $\underline{\mathbf{F}}_{\mathrm{III}}$ is associated with the local solid body acceleration $\underline{\mathbf{a}}$ on ∂B:

$$\underline{\mathbf{F}}_{\mathrm{III}} = \int_{\partial B} \underline{\mathbf{r}} \times (\underline{n} \times \underline{\mathbf{a}})\, \mathrm{d}S \tag{5}$$

The proof of Eqs. (3–5) is based on the so-called derivative moment transformations (DMT) reported in Appendix A.

By exploiting the Helmholtz equation for the vorticity,

$$\frac{\partial \underline{\omega}}{\partial t} + \underline{\nabla} \times \underline{\boldsymbol{l}} = \nu \nabla^2 \underline{\omega} \tag{6}$$

and the transformation (A1), $\underline{\mathbf{F}}_{\mathrm{I}}$ can be cast in an alternative way:

$$\underline{\mathbf{F}}_{\mathrm{I}} = -\int_{\Omega} \left(\underline{\mathbf{r}} \times \frac{\partial \underline{\omega}}{\partial t} \right) \mathrm{d}V - \int_{\Omega} \underline{\boldsymbol{l}}\, \mathrm{d}V - \int_{\partial\Omega} \underline{\mathbf{r}} \times (\underline{n} \times \underline{\boldsymbol{l}})\, \mathrm{d}S \quad \text{(advection form)} \tag{7}$$

named advection form and indicated as $\underline{\mathbf{F}}_{\mathrm{I},a}$. In Eq. (7) the contribution $\underline{\mathbf{F}}_{\mathrm{I}}$ is expressed in terms of time rate of vorticity and Lamb vector integrals. The vortex force, namely, the volume integral of the Lamb vector, appears explicitly in Eq. (7). Since Eq. (6) is true, the diffusion and advection forms are equivalent and represent alternative ways to account for the same flow physics.

III. Aerodynamic Force for High-Reynolds-Number Flows

The equations derived in the previous section require the knowledge of the time varying flowfield. Therefore, the advantage of the theory is restricted to the availability of these data, which are the outcome of direct solutions of the Navier–Stokes equations. In the applications at high-Reynolds-number, the fluid dynamics fields are usually achieved by solving averaged (RANS methods) or spatial filtered equations (large eddy simulation methods). Also in case of experimental measurements the data storage is often made by averaging in time the flow variables. Such processes produce the appearance of extra terms associated with the effects of turbulence. Therefore, a new formulation of the theory of Wu et al. [17] that takes into account averaging processes turns out to be important.

A. Analytical Development

The classical Reynolds decomposition (see Pope [19], p. 83) $\underline{\mathbf{u}} = \langle \underline{\mathbf{u}} \rangle + \underline{\mathbf{u}}'$ is introduced in the RANS equations where $\langle \underline{\mathbf{u}} \rangle$ is the mean velocity and $\underline{\mathbf{u}}'$ is the fluctuation. Different operative definitions of the mean are available, depending on the time scale of the fluid dynamic problem. However, the analytical development of the theory is not affected by a specific averaging procedure. The momentum equation of the mean field is

$$\frac{\partial \langle \underline{\mathbf{u}} \rangle}{\partial t} + \langle \underline{\mathbf{u}} \rangle \cdot \underline{\nabla} \langle \underline{\mathbf{u}} \rangle + \underline{\nabla} \langle p \rangle = \nu \nabla^2 \langle \underline{\mathbf{u}} \rangle + \underline{\nabla} \cdot \underline{\underline{\tau}}^t \tag{8}$$

where $\underline{\underline{\tau}}^t = -\langle \underline{\mathbf{u}}' \underline{\mathbf{u}}' \rangle$ is the Reynolds stress tensor. The same decomposition for the Lamb vector provides

$$\langle \underline{\boldsymbol{l}} \rangle = \langle \underline{\omega} \rangle \times \langle \underline{\mathbf{u}} \rangle + \langle \underline{\boldsymbol{l}}'' \rangle \tag{9}$$

where $\langle \underline{\omega} \rangle = \underline{\nabla} \times \langle \underline{\mathbf{u}} \rangle$, $\underline{\omega}' = \underline{\nabla} \times \underline{\mathbf{u}}'$ and $\langle \underline{\boldsymbol{l}}'' \rangle = \langle \underline{\omega}' \times \underline{\mathbf{u}}' \rangle$. The mean fluctuating Lamb vector $\langle \underline{\boldsymbol{l}}'' \rangle$ is related to the Reynolds stress tensor by the following relation [20]:

$$\langle \underline{\boldsymbol{l}}'' \rangle = -\underline{\nabla} \cdot \underline{\underline{\tau}}^t - \underline{\nabla} \kappa \tag{10}$$

where $\kappa = \langle \underline{\mathbf{u}}' \cdot \underline{\mathbf{u}}' \rangle / 2$ is the turbulent kinetic energy, and the curl of $\langle \underline{\boldsymbol{l}}'' \rangle$ is

$$\underline{\nabla} \times \langle \underline{\boldsymbol{l}}'' \rangle = -\underline{\nabla} \times \underline{\nabla} \cdot \underline{\underline{\tau}}^t \tag{11}$$

By applying the curl operator to the RANS momentum equation, the averaged form of the Helmholtz Eq. (6) is obtained:

$$\frac{\partial \langle \underline{\omega} \rangle}{\partial t} + \underline{\nabla} \times \langle \underline{\boldsymbol{l}} \rangle = \nu \nabla^2 \langle \underline{\omega} \rangle \tag{12}$$

The averaged aerodynamic force $\langle \underline{\mathbf{F}} \rangle$ is obtained using the definition of $\langle \underline{\boldsymbol{l}} \rangle$, the momentum RANS Eqs. (8) and (12) as follows:

$$\langle \underline{\mathbf{F}} \rangle = \langle \underline{\mathbf{F}}_{\mathrm{I}} \rangle + \langle \underline{\mathbf{F}}_{\mathrm{II}} \rangle + \langle \underline{\mathbf{F}}_{\mathrm{III}} \rangle \tag{13}$$

where

$$\langle \underline{\mathbf{F}}_{\mathrm{I},d} \rangle = -\int_{\Omega} \underline{\mathbf{r}} \times (\nu \nabla^2 \langle \underline{\omega} \rangle)\, \mathrm{d}V + \langle \underline{\mathbf{F}}^t \rangle \tag{14}$$

$$\langle \underline{\mathbf{F}}_{\mathrm{II}} \rangle = -\int_{\Sigma} \underline{\mathbf{r}} \times \underline{n} \times \nu(\underline{\nabla} \times \langle \underline{\omega} \rangle)\, \mathrm{d}S + \int_{\Sigma} \nu(\langle \underline{\omega} \rangle \times \underline{n})\, \mathrm{d}S - \langle \underline{\mathbf{F}}^t \rangle \tag{15}$$

$$\langle \underline{\mathbf{F}}_{\mathrm{III}} \rangle = \underline{\mathbf{F}}_{\mathrm{III}} \tag{16}$$

and

$$\langle \underline{\mathbf{F}}^t \rangle = \int_{\Omega} \underline{\mathbf{r}} \times \underline{\nabla} \times \langle \underline{\boldsymbol{l}}'' \rangle\, \mathrm{d}V \tag{17}$$

is an explicit additional turbulent term. The averaged advection form is

$$\langle \underline{\mathbf{F}}_{\mathrm{I},a} \rangle = -\int_{\Omega} \underline{\mathbf{r}} \times \frac{\partial \langle \underline{\omega} \rangle}{\partial t}\, \mathrm{d}V - \int_{\Omega} \langle \underline{\boldsymbol{l}} \rangle\, \mathrm{d}V - \int_{\partial\Omega} \underline{\mathbf{r}} \times \underline{n} \times \langle \underline{\boldsymbol{l}} \rangle\, \mathrm{d}S + \langle \underline{\mathbf{F}}^t \rangle \tag{18}$$

Since the term $\langle \underline{\mathbf{F}}^t \rangle$ appears with the plus sign in both the Eqs. (14) and (18) and with the minus sign in Eq. (15), the mean total aerodynamic force $\langle \underline{\mathbf{F}} \rangle$ does not depend on it. The final expression of the averaged aerodynamic force is formally the same derived by Wu et al. [17] for the Navier–Stokes equations, provided that the instantaneous field is replaced with its average. However, here the single contributions $\langle \underline{\mathbf{F}}_{\mathrm{I}} \rangle$ and $\langle \underline{\mathbf{F}}_{\mathrm{II}} \rangle$ have an additional term depending on the turbulent fluctuations.

In a practical application the diffusion form has the advantage that all integrals can be computed by means of the average vorticity $\langle \underline{\omega} \rangle$ only. An important drawback is the involvement of the third spatial derivatives of the velocity field which are more difficult to compute

accurately. However, the advection form only requires the first order spatial derivatives of the velocity. In addition, the vortex force term appears explicitly only in the advection form. For these reasons such form will be adopted in the present paper.

B. Some Remarks

The computation of the aerodynamic force using the sum $\langle \underline{\mathbf{F}}_{\mathrm{I},a} \rangle + \langle \underline{\mathbf{F}}_{\mathrm{II}} \rangle + \langle \underline{\mathbf{F}}_{\mathrm{III}} \rangle$ does not require the explicit knowledge of $\langle \underline{\mathbf{F}}^t \rangle$. However, the Reynolds stress tensor $\underline{\underline{\tau}}^t$ and turbulent kinetic energy κ are involved in the computation of $\langle \underline{\boldsymbol{l}} \rangle$ by Eqs. (9) and (10). An alternative way is to compute $\langle \underline{\mathbf{F}}_{\mathrm{I},a} \rangle$ in terms of the mean velocity $\langle \underline{\mathbf{u}} \rangle$ and vorticity $\langle \underline{\omega} \rangle$ as follows:

$$\langle \underline{\mathbf{F}}_{\mathrm{I},a} \rangle = -\int_\Omega \underline{\mathbf{r}} \times \frac{\partial \langle \underline{\omega} \rangle}{\partial t}\, \mathrm{d}V - \int_\Omega \langle \underline{\omega} \rangle \times \langle \underline{\mathbf{u}} \rangle\, \mathrm{d}V - \int_{\partial\Omega} \underline{\mathbf{r}} \times \underline{n} \times (\langle \underline{\omega} \rangle \times \langle \underline{\mathbf{u}} \rangle)\, \mathrm{d}S \tag{19}$$

The advection form is correctly computed by using Eq. (19), but, as a consequence, the need to calculate $\langle \underline{\mathbf{F}}^t \rangle$ in $\langle \underline{\mathbf{F}}_{\mathrm{II}} \rangle$ now arises. A dimensional analysis based on the boundary-layer theory, reported in appendix B, shows that the contribution $\langle \underline{\mathbf{F}}_{\mathrm{II}} \rangle$ is negligible for high-Reynolds and wall bounded flows. The same analysis holds for turbulent boundary-layer flows, except for the term $\langle \underline{\mathbf{F}}^t \rangle$. However, by choosing a proper control volume Ω, as discussed in appendix C, the computation of $\langle \underline{\mathbf{F}}^t \rangle$ can be avoided.

The two-dimensional advection form (19) and the body surface contribution (5) can be explicated in an orthogonal Cartesian reference system Oxy. The expressions of lift and drag coefficients are obtained by assuming the x axis parallel to the free stream velocity U_∞, and dividing by $U_\infty^2 c/2$:

$$C_l = \underbrace{-2\int_\Omega \langle \omega \rangle \langle u \rangle\, \mathrm{d}V}_{(C_l)_\Omega} + \underbrace{2\int_\Omega x \langle \dot{\omega} \rangle\, \mathrm{d}V}_{(C_l)_{\dot{\omega}}} + \underbrace{2\int_\Sigma x \langle \omega \rangle \langle \underline{\mathbf{u}} \rangle \cdot \underline{n}\, \mathrm{d}S}_{(C_l)_\Sigma} - \underbrace{2\int_{\partial B} x a_B\, \mathrm{d}S}_{(C_l)_B} \tag{20a}$$

$$C_d = \underbrace{2\int_\Omega \langle \omega \rangle \langle v \rangle\, \mathrm{d}V}_{(C_d)_\Omega} \underbrace{-2\int_\Omega y \langle \dot{\omega} \rangle\, \mathrm{d}V}_{(C_d)_{\dot{\omega}}} \underbrace{-2\int_\Sigma y \langle \omega \rangle \langle \underline{\mathbf{u}} \rangle \cdot \underline{n}\, \mathrm{d}S}_{(C_d)_\Sigma} + \underbrace{2\int_{\partial B} y a_B\, \mathrm{d}S}_{(C_d)_B} \tag{20b}$$

where $\langle u \rangle$ and $\langle v \rangle$ are the Cartesian components of $\langle \underline{\mathbf{u}} \rangle$, $\langle \underline{\omega} \rangle = \langle \omega \rangle \underline{k}$, $\langle \dot{\omega} \rangle$ is the time derivative of $\langle \omega \rangle$ and $a_B = |\underline{n} \times (\underline{\mathbf{a}} - \underline{\boldsymbol{l}})|$. Each term of Eqs. (20a) and (20b) has been labeled for an easier discussion in the applications. In case of unsteady periodic RANS solutions, the quantities in Eqs. (20) must be considered as phase averages, which are the direct outcome of the unsteady RANS based CFD solvers.

IV. Results and Discussion

The CFD solutions have been obtained using a standard finite volume method solving the compressible RANS equations [21] at low Mach numbers. The spatial discretization is a second order scheme based on a cell-centered formulation with an explicit artificial dissipation model. The relaxation operator is a multistage Runge–Kutta integration scheme. The unsteady computations are carried out by a second order accurate formula. The turbulent calculations are performed through a RANS approach with the turbulent nonturbulent κ-ω model of Kok [22] and the shear stress transport model of Menter [23]. A two dimensional C-type structured grid around the NACA0012 airfoil has been created with 768×200 cells in streamwise and normal wise directions, respectively. The outer boundary is located at about 30 chord units from the airfoil surface. The integrals are numerically computed using the cell-centered data of the flow solver output. The data are considered as averages over the cell volume, which is consistent with the discretization of the flow equations.

Two kinds of applications are presented. First, steady RANS solutions are analyzed for several Reynolds numbers and angles of attack. Then the unsteady turbulent flows around the oscillating airfoil are examined.

A. Steady RANS Flows

Three Reynolds numbers have been investigated, $Re = 1.0 \times 10^6$, 5.0×10^6, and 1.0×10^7 at angles of attack $0° \le \alpha \le 6°$ at free stream Mach number 0.1. Fully turbulent flow condition are considered in all the computations. As a reference, the $C_{l\alpha}$ and the C_d at $\alpha = 0°$ obtained from the standard near-field integration are compared with some experimental data [24] in Fig. 2.

The far-field form of the aerodynamic force expressed by Eqs. (20) does not depend on the volume Ω selected for the integral calculations. Nevertheless some dependencies are expected when we deal with the numerical solutions. Furthermore, the single contributions can vary according to the position assumed by the surface Σ in the flowfield. An integration domain Ω based on a typical computational grid for CFD calculations is proposed in Fig. 3. The surface Σ is defined as $\Sigma_I \cup \Sigma_J$, where Σ_I is obtained by selecting a grid line of the computational mesh with a constant index i, and Σ_J with a constant index j. The surface Σ_I intersects the airfoil wake at a distance x_S from the trailing edge while the surface Σ_J is located at y_S from the solid surface. In the following, the normalized aerodynamic coefficients, $(C_l)^*$ and $(C_d)^*$, defined as the ratio

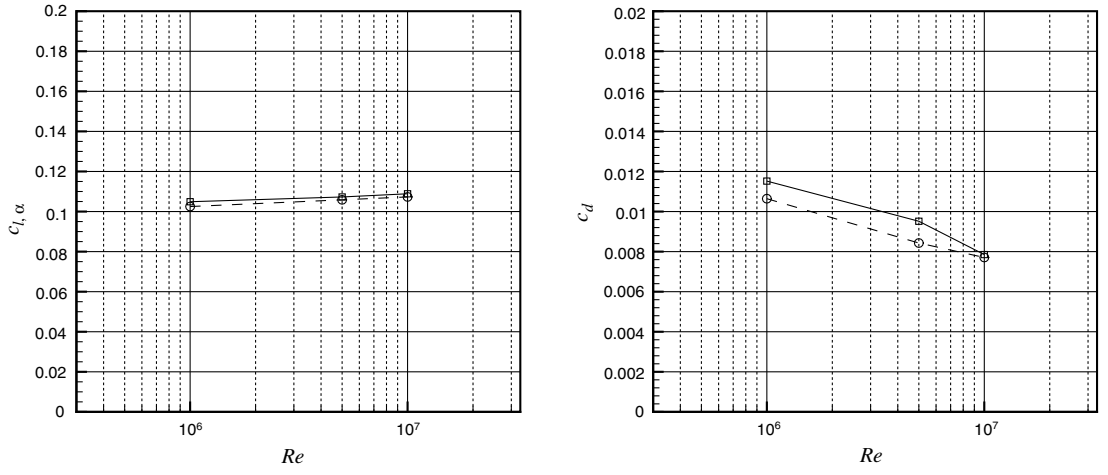

Fig. 2 NACA0012 airfoil, turbulent steady flow solutions: a) $dC_l/d\alpha$ and b) C_d at $\alpha = 0°$. □, computations; and ° experiments [24].

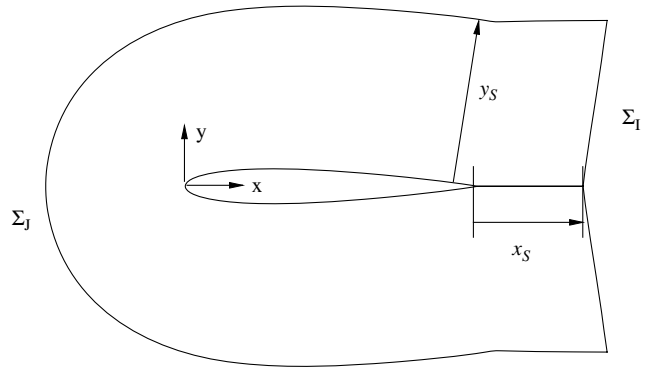

Fig. 3 Integration domain Ω limited by the surfaces Σ_I and Σ_J.

of the far-field coefficient by the corresponding near-field one, are used:

$$(C_l)^* = \frac{(C_l)_{\text{Far field}}}{(C_l)_{\text{Near field}}}; \qquad (C_d)^* = \frac{(C_d)_{\text{Far field}}}{(C_d)_{\text{Near field}}}$$

where the superscript * specifies the normalization operation.

1. Effects of the Σ_I Location

In Fig. 4a the normalized lift coefficients are reported for several Reynolds numbers and angles of attack by increasing the x_S location of the Σ_I surface from zero to $25c$ downstream the airfoil. The surface Σ_J is located at a distance $y_S \approx 15c$. The contributions related to the volume integral $(C_l)^*_\Omega$, Fig. 4b, and the surface contributions $(C_l)^*_{\Sigma_I}$ and $(C_l)^*_{\Sigma_J}$, Figs. 4c and 4d, are plotted separately. Although the curves refer to different α and Reynolds numbers, no significant dependency on these parameters is visible. The $(C_l)^*$ is ≈ 1 within a narrow band of 2% while the vortex force and the surface contributions, $(C_l)^*_\Omega$ and $(C_l)^*_{\Sigma_I}$, vary linearly compensating each other. A constant term is obtained from the surface integral on Σ_J. The variation of $(C_l)^*_{\Sigma_I}$ with x_S is an effect of the external boundary conditions on the lift. In fact, with a more extended CFD domain of about $100c$, it has been proved that the surface contributions $(C_l)^*_{\Sigma_I}$ and $(C_l)^*_{\Sigma_J}$ vanish and $(C_l)^*_\Omega \approx 1$ (see Appendix D).

In Fig. 5a the normalized drag coefficients at $\alpha = 0°$ are reported. The drag coefficient computed by the formula (20), agrees with the near-field data up to $x_S \approx 10c$. The 25% of uncertainty on the normalized drag coefficient is equivalent to about 30 drag counts at Reynolds 10^6, and to 19 drag counts at Reynolds 10^7. The volume contribution $(C_d)_\Omega \to 0$ as x_S increases, Fig. 5b, and the main part of the drag remains associated with the surface contribution $(C_d)_{\Sigma_I}$, as shown in Fig. 5c. The contribution $(C_d)_{\Sigma_J}$, (Fig. 5d), provides a constant term. As $x_S \to \infty$ it is possible to proof that $(C_d)_{\Sigma_I}$ reduces to the well known formula of the wake drag [25], as already shown by Wu [14]. In fact, by assuming a boundary-layer approximation, it is straightforward to verify that

$$\lim_{x_s \to \infty} (C_d)_{\Sigma_I} = C_d = 2\theta_\infty$$

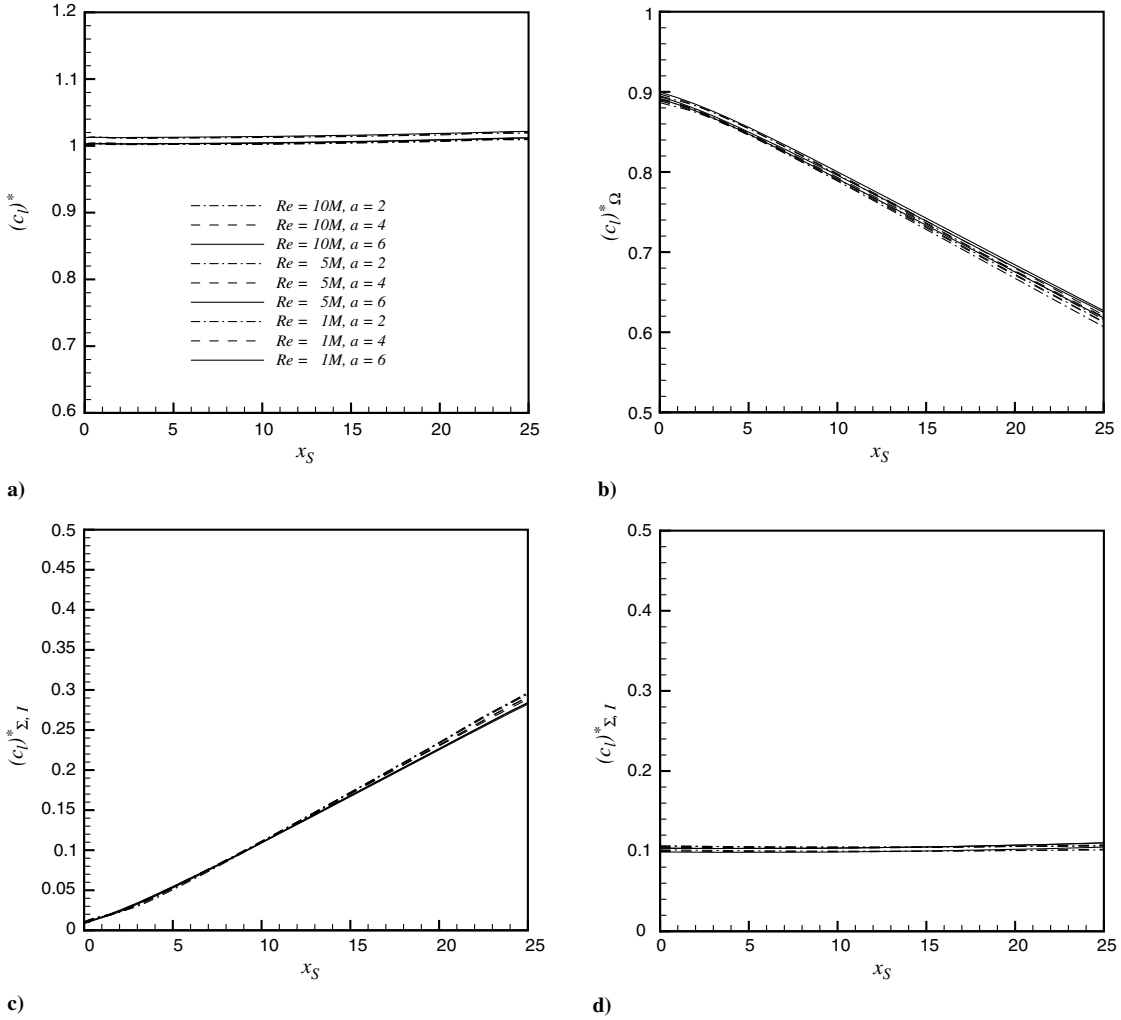

Fig. 4 Turbulent flow solutions at Reynolds numbers 1.0×10^6, 5.0×10^6 and 1.0×10^7. Angles of attack $\alpha = 2, 4$ and 6°. Normalized contributions of lift coefficients by varying the Σ_I position: a) $(C_l)^*$, b) volume contribution $(C_l)^*_\Omega$, c) surface contribution $(C_l)^*_{\Sigma_I}$, and d) surface contribution $(C_l)^*_{\Sigma_J}$.

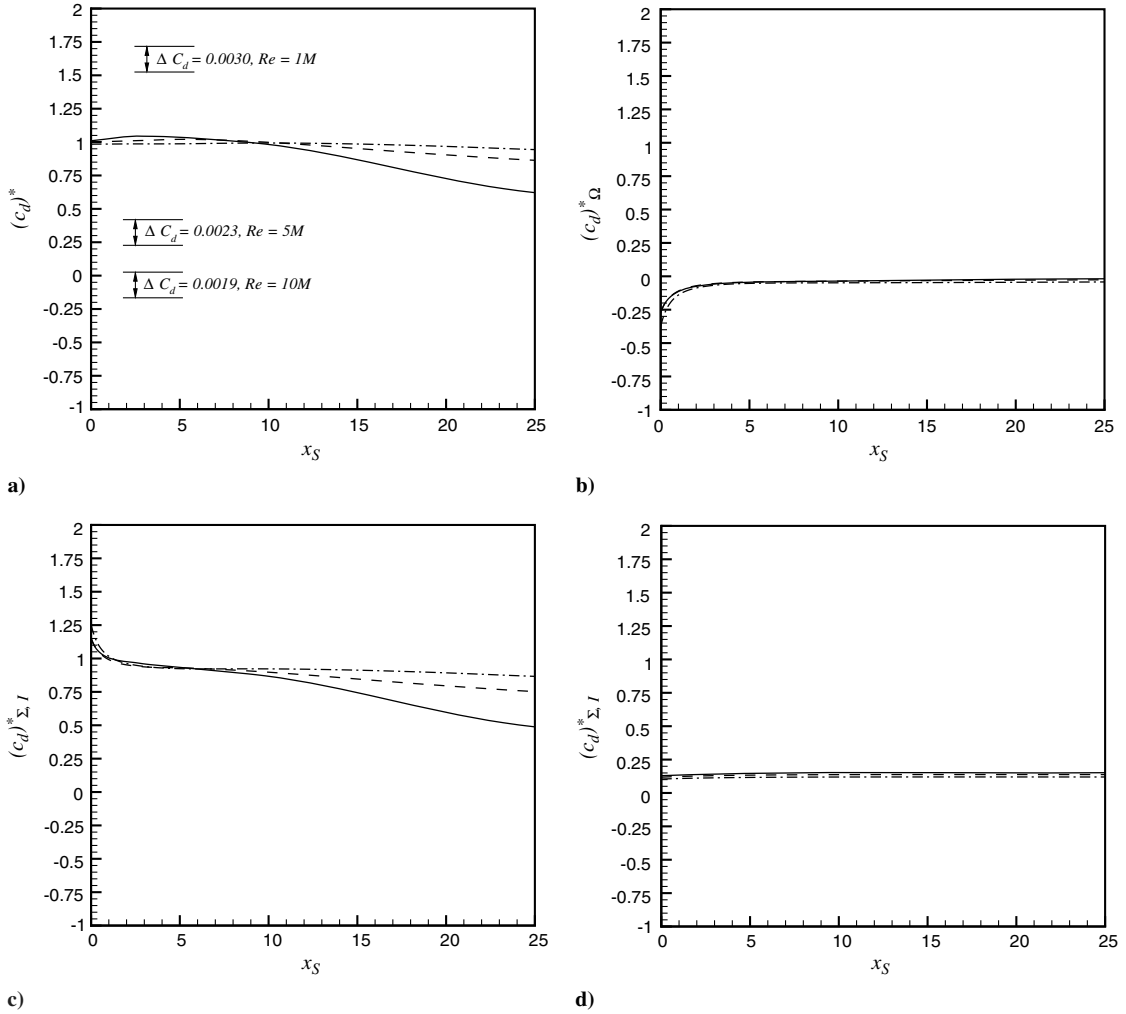

Fig. 5 Turbulent flow solutions at $\alpha = 0°$. Normalized contributions of drag coefficients by varying Σ_I position. Dotted-dashed line, $Re = 1.0 \times 10^6$; dashed line, $Re = 5.0 \times 10^6$; and solid line, $Re = 1.0 \times 10^7$: a) $(C_d)^*$, b) volume contribution $(C_d)^*_\Omega$, c) surface contribution $(C_d)^*_{\Sigma_I}$, and d) surface contribution $(C_d)^*_{\Sigma_J}$.

where θ_∞ is the momentum thickness computed in the wake infinitely downstream. As a consequence, when Σ_I is located far downstream of the airfoil, the drag coefficient accuracy is mainly affected by the quality of the CFD solution in the wake, which is usually not sufficient after few chords downstream. This aspect has been highlighted by exploiting the self-similar behavior of the turbulent wakes behind no lifting bodies (see Appendix E). In Figs. 6a and 6b, the flow velocity defect of the numerical solution at $\alpha = 0°$ at two stations in the wake ($x = 3c$, and $x = 15c$) is compared with the theoretical self-similar curve. The agreement is a good for

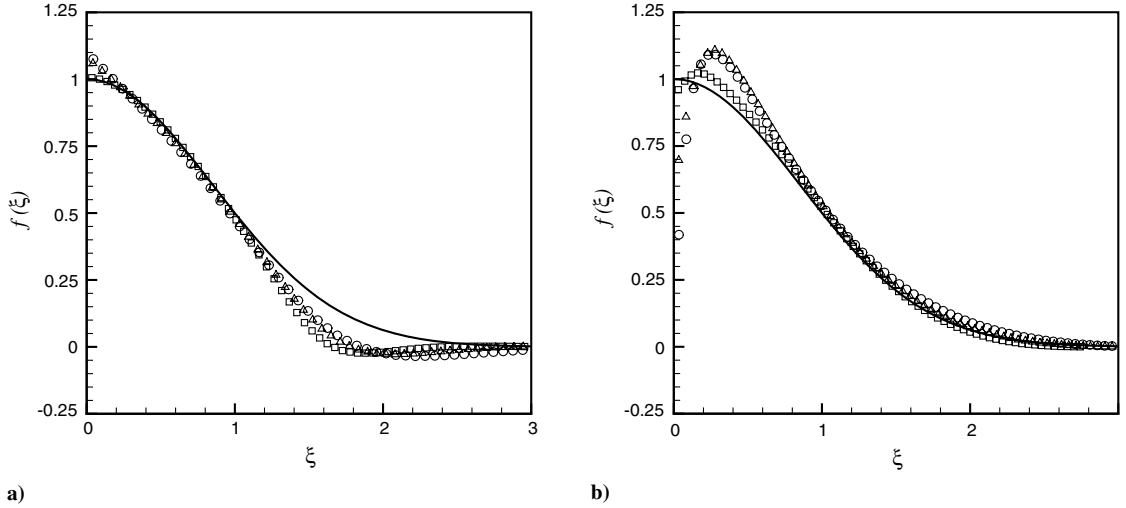

Fig. 6 Turbulent flow solutions at $\alpha = 0°$. Normalized velocity defect $f(\xi)$ in the wake versus the self-similar variable ξ. (Appendix E). □, $Re = 1.0 \times 10^6$; △, $Re = 5.0 \times 10^6$; ° $Re = 1.0 \times 10^7$; and solid line, analytic: a) $x/c = 3$ and b) $x/c = 15$.

$x = 3c$; however, the velocity profile is completely wrong, even in the shape, for $x = 15c$. This behavior is responsible of the not correct drag prediction for $x > 10c$.

2. *Effects of the Σ_J Location*

In this section the effects of moving the Σ_J surface on the wall normal direction are analyzed. The Σ_I surface is at $x_S = 0.004c$ after the airfoil trailing edge. In Fig. 7a, the lift coefficient contributions are reported as function of y_S. The logarithmic scale is used to highlight the turbulent viscous layer. The integrals converge towards the near-field values for y_S greater than the boundary-layer thickness. No dependency is visible on α and Re once convergence is achieved. It has also to be noted in Fig. 7b that for y_S greater than the boundary-layer thickness, $(C_l)^*_\Omega \to 1$, whereas, in Figs. 7c and 7d the normalized surface contributions $(C_l)^*_{\Sigma_I}$ and $(C_l)^*_{\Sigma_J} \to 0$. For $y_S > 10c$ an effect of the numerical boundary conditions is visible on $(C_l)^*_\Omega$ and $(C_l)^*_{\Sigma_J}$. For $y_S \leq 10^{-1}$, large overshoots are obtained because of the neglected terms associated with the turbulent and laminar shear stress components. The diagrams of the drag coefficients are reported in Figs. 8a–8d. The C_d contributions are correctly computed by increasing the distance y_S beyond the boundary-layer. It can also be noted that for the selected domain the surface contribution $(C_d)^*_{\Sigma_I}$ tends to 1.45, and $(C_d)^*_\Omega \to -0.55$. These values depend on the distance of the surface Σ_I from the airfoil as already seen from the C_d diagrams in Fig. 5.

A calculation of the terms involved in the expression of $\langle \underline{\mathbf{F}}_{\mathrm{II}} \rangle$, Eq. (15), is presented. For this purpose, a new refined grid of 768×400 cells, with about 200 points within the boundary-layer thickness was used. When the surface Σ_J intersects the boundary layer, the viscous and turbulent terms in Eq. (15) need to be computed in order to obtain the agreement with the near-field results. From an analytical point of view, when $\Sigma \to \partial B$, the volume integrals $\langle \underline{\mathbf{F}}_{\mathrm{I}} \rangle \to 0$ and all the aerodynamic force reduces to $\langle \underline{\mathbf{F}}_{\mathrm{II}} \rangle$. The extreme case in which $\Sigma = \partial B$ the classical near-field form is recovered. In the intermediate region, the Reynolds stress tensors, expressed by $\langle \underline{\mathbf{F}}^T \rangle$ have to be taken into account. By using the DMT (A1) and the relation (11), the integral $\langle \underline{\mathbf{F}}^t \rangle$ in Eq. (17) can be cast in two surface integrals:

$$\langle \underline{\mathbf{F}}^t \rangle = -\int_\Sigma \underline{\mathbf{r}} \times \underline{n} \times \underline{\nabla} \cdot \underline{\underline{\tau}}^t \, \mathrm{d}S - \int_\Sigma \underline{\underline{\tau}}^t \cdot \underline{n} \, \mathrm{d}S \tag{21}$$

Therefore, the complete expression of $\langle \underline{\mathbf{F}}_{\mathrm{II}} \rangle$ is

$$\langle \underline{\mathbf{F}}_{\mathrm{II}} \rangle = \underbrace{\int_\Sigma \underline{\mathbf{r}} \times \underline{n} \times \underline{\nabla} \cdot (\underline{\underline{\tau}} + \underline{\underline{\tau}}^t) \, \mathrm{d}S}_{A} + \underbrace{\int_\Sigma \underline{\underline{\tau}}^t \cdot \underline{n} \, \mathrm{d}S}_{B} + \underbrace{\int_\Sigma \underline{\underline{\tau}} \cdot \underline{n} \, \mathrm{d}S}_{C} \tag{22}$$

These contributions have been plotted for a case at $Re = 10^6$ and $\alpha = 2°$ in Figs. 9a and 9b. The coordinate of the surface Σ_J has been reported in wall units (y_S^+) at the trailing edge of the airfoil. The classical regions of a turbulent boundary-layer (defined in terms of y^+ [19]) have also been highlighted. The normalized lift and drag coefficients are now correctly computed up to the solid wall. The

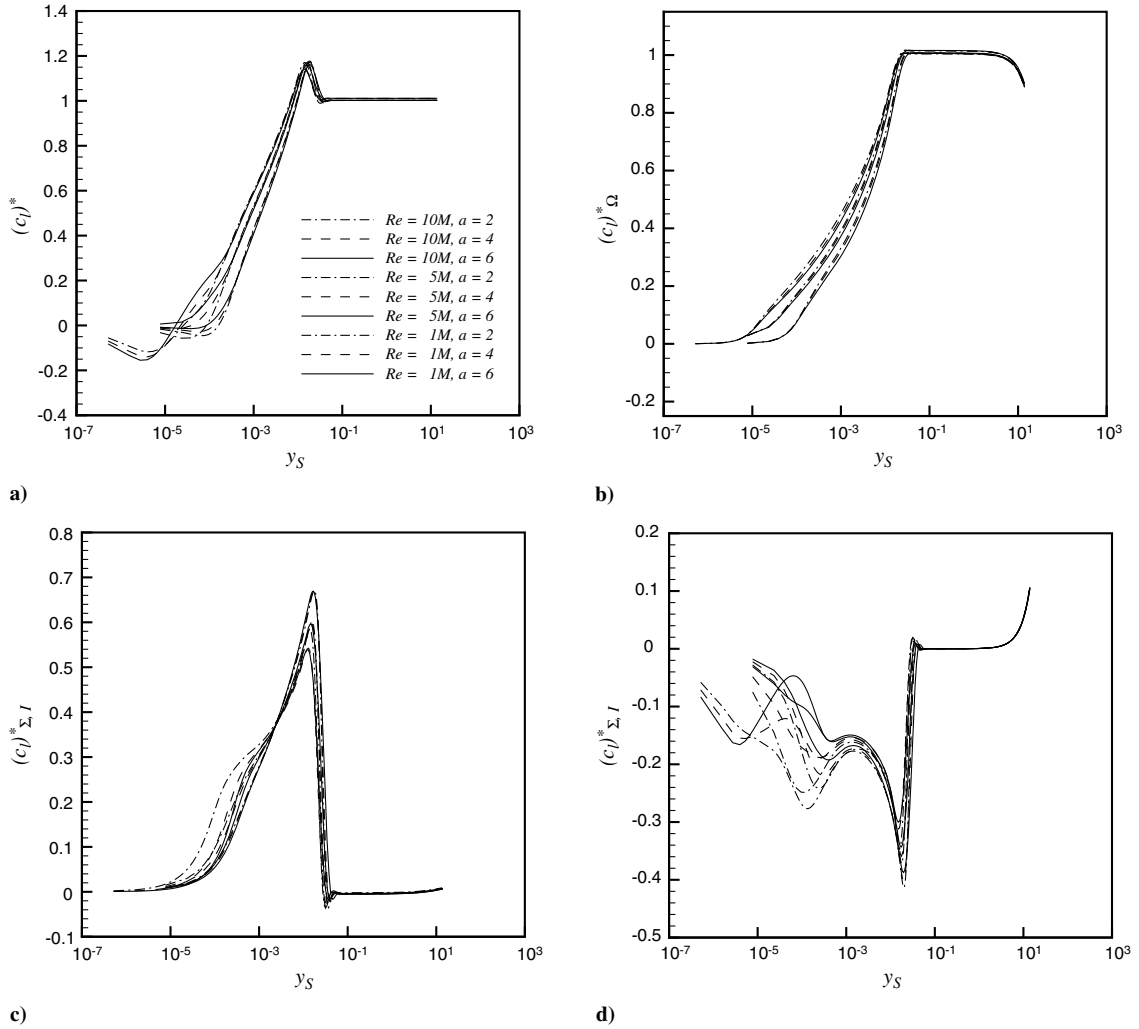

Fig. 7 Turbulent flow solutions at Reynolds numbers 1.0×10^6, 5.0×10^6 and 1.0×10^7. Angles of attack $\alpha = 2$, 4 and 6°. Normalized contributions of lift coefficients by varying Σ_J position: a) sum of all contributions $(C_l)^*$, b) volume contribution $(C_l)^*_\Omega$, c) surface contribution $(C_l)^*_{\Sigma_I}$, and d) surface contribution $(C_l)^*_{\Sigma_J}$.

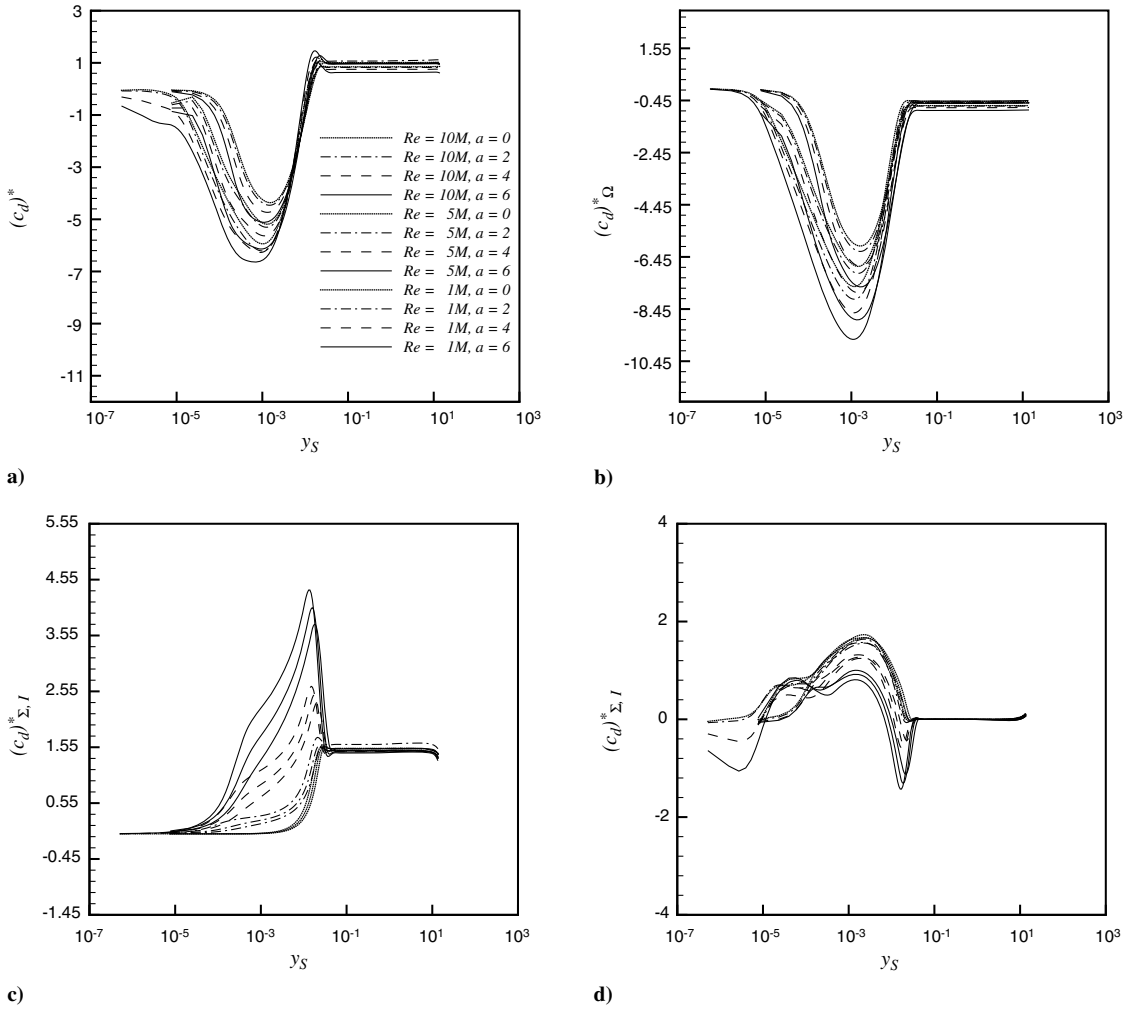

Fig. 8 Turbulent flow solutions at Reynolds numbers: 1.0×10^6, 5.0×10^6 and 1.0×10^7. Angles of attack: $\alpha = 0, 2, 4$ and $6°$. Normalized contributions of drag coefficients by varying Σ_J position: a) sum of all contributions $(C_d)^*$, b) volume contribution $(C_d)^*_\Omega$, c) surface contribution $(C_d)^*_{\Sigma_I}$, and d) surface contribution $(C_d)^*_{\Sigma_J}$.

contribution A takes into account the dynamic part of the boundary layer and balances the Lamb vector integral. A tends to zero outside the boundary layer and provides the pressure part of the lift and drag at the solid wall. The Reynolds stress tensor term B allows to identify the logarithmic layer as well as the end of the turbulent boundary layer. The buffer layer, in which the turbulent fluctuations are the same order of magnitude of the laminar terms, is recognizable as the region in which B and C compensate. Finally, in the viscous sub layer, the dominance of the laminar viscosity is visible. The term C provides the viscous part of the lift and drag at the solid wall.

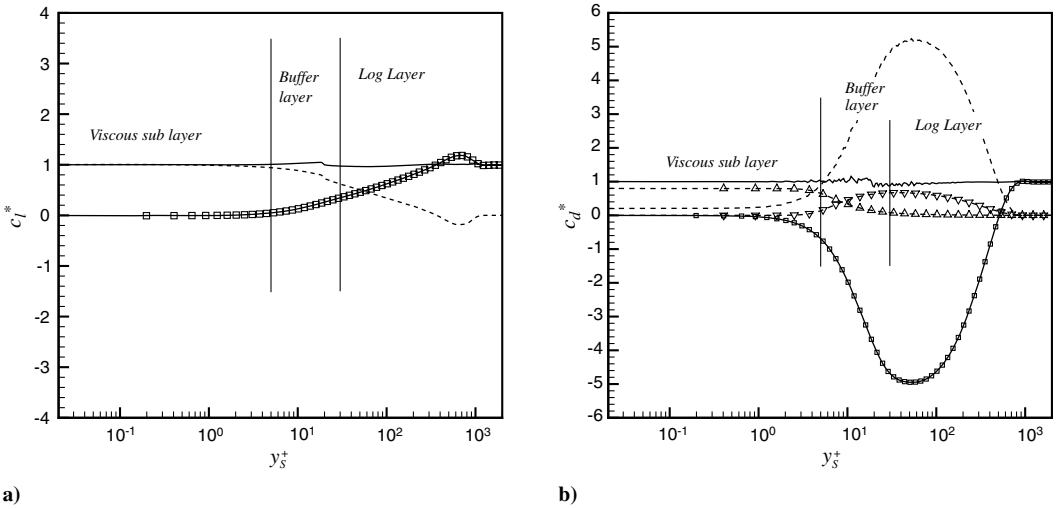

Fig. 9 Turbulent flow solutions at Reynolds number 1.0×10^6 and $\alpha = 2°$. Normalized contributions of lift and drag coefficients by varying Σ_J position in the boundary layer: a) $(C_l)^*$ and b) $(C_d)^*$. Solid line, sum of all contributions; -□-, Lamb vector integrals [Eq. (20)]; dashed line, (A); -∇-, (B); and -△-, (C). See Eq. (22) for the labels.

3. Observations

The effects of the variation of Ω on the computed aerodynamic coefficients have been discussed for several steady RANS solutions around a two dimensional airfoil. It has been shown that the lift coefficient reduces to the Lamb vector volume integral, namely, to the vortex force, by increasing the dimension of Ω. Analogously, the drag coefficient reduces to a surface integral on the wake. Namely,

$$\lim_{(x_S,y_S)\to\infty}(C_l)_\Omega = C_l \qquad \lim_{(x_S,y_S)\to\infty}(C_d)_{\Sigma_I} = C_d$$

However, as Ω collapses to the solid body surface, the Eqs. (20) are no longer able to predict the aerodynamic force and the turbulent and viscous terms have to be computed. From a numerical point of view, the most favorable condition has been obtained for $x_S \sim 0$ and y_S greater than the boundary-layer thickness. In this way, $\langle \underline{\mathbf{F}}_{\mathrm{II}} \rangle$ results negligible and its computation can be avoided.

B. Unsteady RANS Applications

The application of the present far-field method to an unsteady flow solution permits to estimate the effects of the time derivative of the vorticity field and of the body acceleration. As pointed in the previous section, phase averages of the flow variables are considered in Eqs. (20). A CFD solution of the flow around the NACA0012 airfoil has been obtained at a Reynolds number $Re = 1.35 \cdot 10^5$. A sinusoidal variation of the angle of attack $\alpha = 7.5° \sin(2kt)$, with a reduced frequency $k = \omega c/2U_\infty = 0.05$ has been imposed. The pitching axis is fixed at $(0.25c, 0)$. The time step of the CFD solution has been chosen by subdividing the oscillating period T into 1024 steps. A periodic solution is obtained after a simulated time equal to $4T$.

On the basis of the results of the previous section, the integration domain Ω used for the far-field force decomposition has been fixed with $x_S \simeq 0.004c$ and $y_S \simeq 15c$. The volume integrals of the vorticity time derivative, $(C_l)_{\dot\omega}$ and $(C_d)_{\dot\omega}$, are calculated by means of a second order central formula in time, while the body surface integrals, $(C_l)_B$ and $(C_d)_B$, are known since the body motion is rigid. In particular we have

$$\underline{\mathbf{a}}_B = (\underline{\mathbf{a}} - \underline{\boldsymbol{l}})_B = -\ddot\alpha\, \underline{k} \times (\underline{B} - \underline{O}) + \dot\alpha^2 (\underline{B} - \underline{O})$$

where $\underline{B} \in \partial B$ and $\underline{O}$ is the location of the pitching axis. In Fig. 10 the hysteresis curves of the lift and drag coefficients are reported as function of the instantaneous incidence for both the near-field and far-field formulations. A very good agreement has been achieved. This result confirms that Eqs. (20) are able to reproduce the unsteady aerodynamic force in case of a turbulent flow around an oscillating airfoil.

The unsteady breakdown of the aerodynamic coefficients is discussed. The body acceleration contribution a_B is quite small compared with the others because of the low value of the reduced frequency k. In Fig. 11 the aerodynamic coefficients $(C_l)_{\Sigma_I}$ and

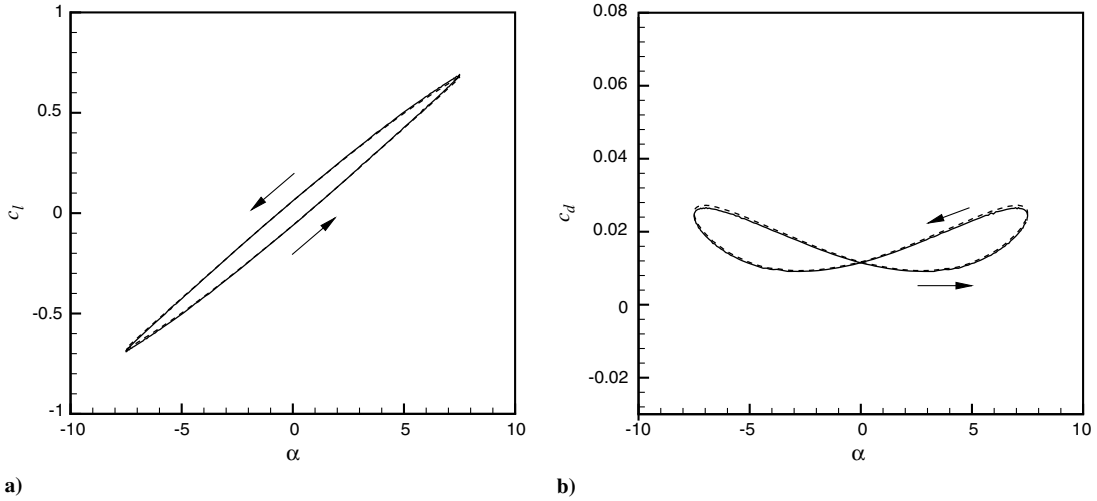

Fig. 10 Unsteady turbulent flow solution around the oscillating airfoil. $\alpha = 7.5° \sin(2kt)$, $k = 0.05$ and $Re = 1.35 \times 10^5$. Aerodynamic coefficient cycles. Dashed line, near-field method; and solid line, far-field method: a) C_l and b) C_d.

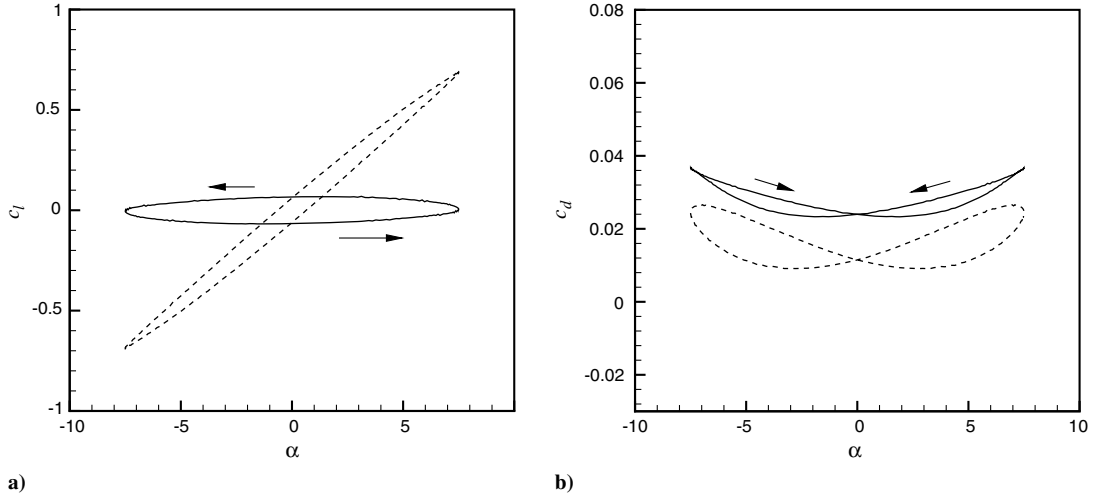

Fig. 11 Unsteady turbulent flow solution around the oscillating airfoil. $\alpha = 7.5° \sin(2kt)$, $k = 0.05$ and $Re = 1.35 \times 10^5$. Aerodynamic coefficient cycles. Dashed line, near-field method; and solid line, free vorticity contributions: a) C_l and b) C_d.

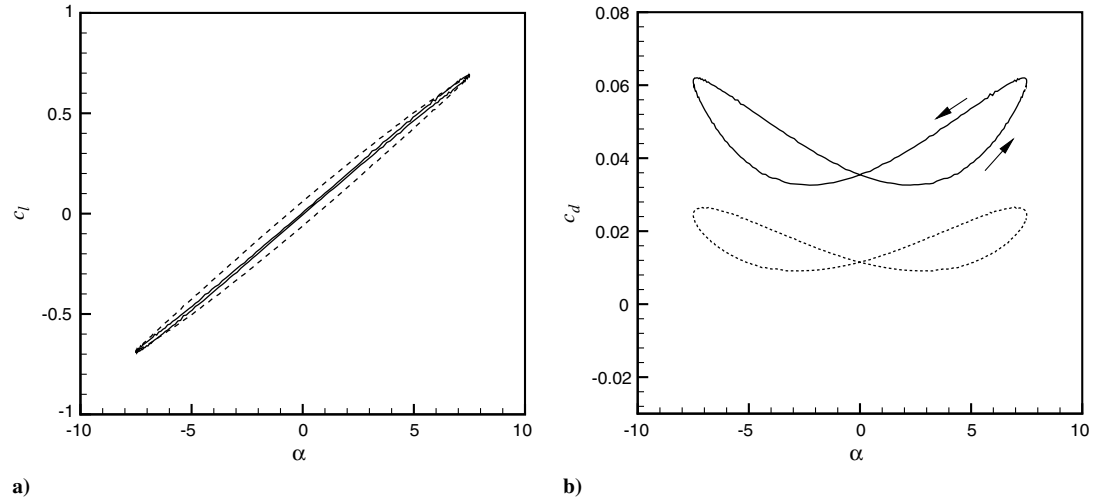

Fig. 12 Unsteady turbulent flow solution around the oscillating airfoil. $\alpha = 7.5° \sin(2kt)$, $k = 0.05$ and $Re = 1.35 \times 10^5$. Aerodynamic coefficient cycles. Dashed line, near-field method; and solid line, bound vorticity contributions: a) C_l and b) C_d.

$(C_d)_{\Sigma_I}$ computed on the wake surface Σ_I are plotted versus the angle of attack. They take into account the unsteady effects of the vorticity shed in the wake just through the Σ_I surface. The recognition of such contribution allows for the identification of a basic mechanism of the unsteady aerodynamics, namely, the breakdown of the force in free $\underline{\omega}^f$ and bound vorticity $\underline{\omega}^b$ parts. The last one is represented by the vorticity created in the boundary layer while the former is associated with the vorticity shed in the wake. To detect such contributions, it is worth noting that the lift C_l^f produced by the free vorticity $\underline{\omega}^f$ is obtained by integrating over a domain Ω that leaves out the bound vorticity layer. For difference, the bound vorticity contribution C_l^b is $C_l - C_l^f$. The aerodynamic coefficients associated with bound

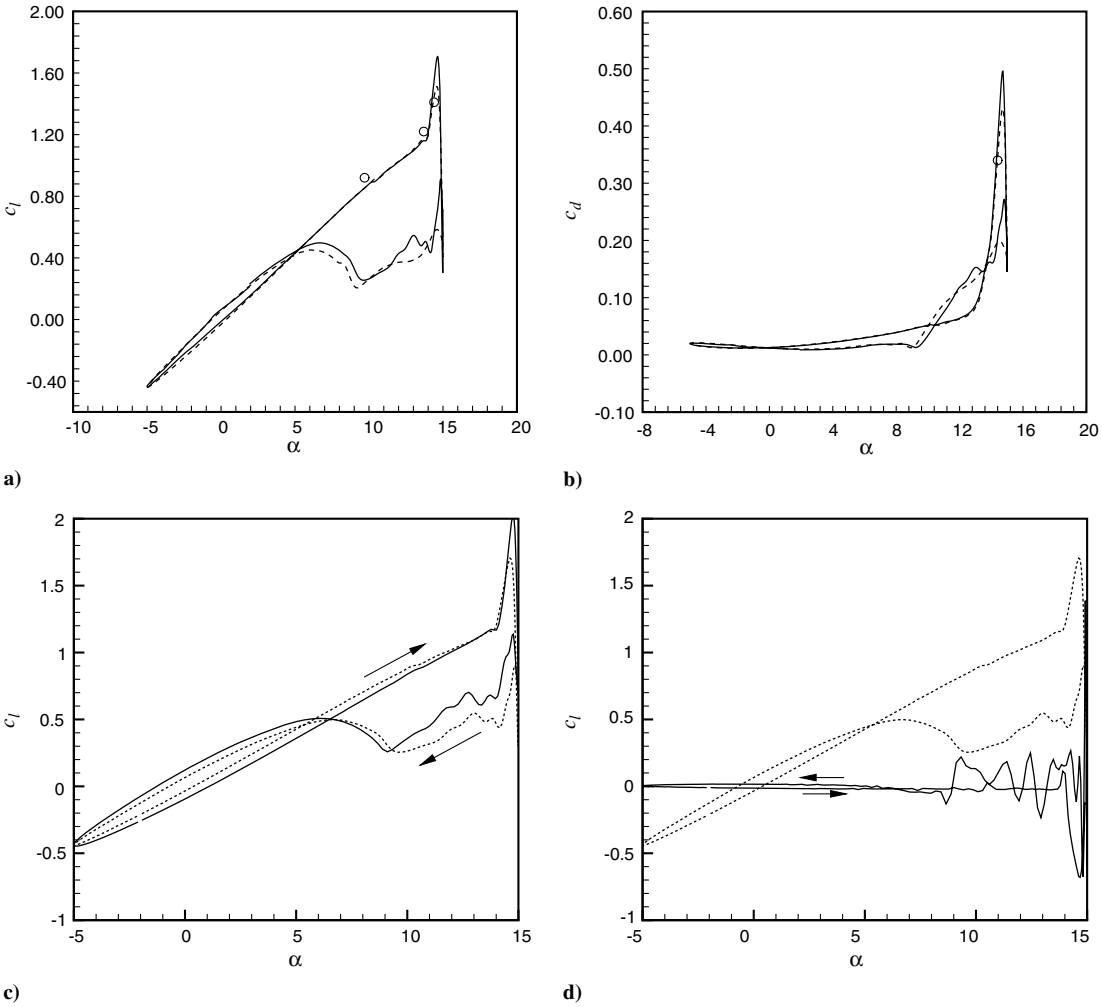

Fig. 13 Unsteady turbulent flow solution around the oscillating airfoil. $\alpha = 5° + 10° \sin(2kt)$. $k = 0.05$. $Re = 1.35 \times 10^5$. Aerodynamic coefficient cycles. Dashed line, near-field method; solid line, far-field method, partial contributions; and °, experimental data [26]: a) C_l, b) C_d, c) $(C_l)_\Omega$, and d) $(C_l)_{\dot{\omega}}$.

vorticity are visible in Fig. 12. The bound vorticity lift coefficient C_l^b is practically in phase with the airfoil angular position α, while the same decomposition applied to the drag coefficient leads to a shift of the hysteresis cycle toward higher values.

The robustness of the present far-field method has been tested also for a dynamic-stall flow. In this case, the oscillation motion is such to overcome the static stall angle resulting in the periodic formation of wide zones of separated flow. One of the main concerns is the generation of an extra lift (with respect to the static stall) caused by the formation and convection of the dynamic-stall vortex. In this case, the far-field form (20) is used as post processing tool to demonstrate the role of the vorticity in such a complex flow. The dynamic stall is obtained by imposing the pitching motion law $\alpha = 5^\circ + 10^\circ \sin(2kt)$, with a reduced frequency $k = 0.05$ at Reynolds number $Re = 1.35 \cdot 10^5$. Some experimental points from the work of Lee and Gerontakos [26] have also been reported as a reference.

In Figs. 13a and 13b the lift and drag coefficients obtained from Eqs. (20) are compared with the near-field data. They are plotted as function of α. The very good agreement of the two formulations confirms that the viscous and turbulent terms associated with the integrals $\langle \underline{\mathbf{F}}_{\mathrm{II}} \rangle$ can be neglected also in case of an unsteady computation, as long as the integration surface is selected outside the boundary layer.

In the Figs. 13c and 13d, an example of the lift coefficient breakdown is made by extracting the Lamb vector integral $(C_l)_\Omega$, (Fig. 13c), and the unsteady vorticity term, $(C_l)_{\dot{\omega}}$, Fig. 13d. As for the previous test, the solid body acceleration is negligible. The Lamb vector integral (vortex force) takes into account the main part of the total lift and is responsible for the slope of the lift hysteresis cycle. However, the remaining contributions associated with the vortex shedding in the wake have a minor role excepted during the stalled part of the cycle, where strong oscillations are visible. In Fig. 13d, the peaks visible on the $(C_l)_{\dot{\omega}}$ curve, point out the detachment and the convection of vorticity downstream the airfoil. Such oscillations increase during the reattachment phase but do not appear in the C_l curve because are compensated by the surface integral on Σ_I (not showed here for shortness).

From the analysis of such integrals it is possible to extract useful information on the dynamics of the stall vortex such as its strength and convection speed.

V. Conclusions

In this paper, it has been proposed a far-field analysis of the aerodynamic force acting on an airfoil in steady and unsteady turbulent conditions.

The theory on which such analysis is founded, was initially developed for flows governed by the unsteady Navier–Stokes equations. In the present paper the theory has been extended to high-Reynolds-number flows. In particular, for turbulent flows the theory has been made suitable for the RANS equations. Several kinds of applications have been discussed.

The extension of the theory to turbulent flows has permitted to deal with numerical solutions governed by the RANS equations. It has been shown that in case of laminar boundary-layer approximation, some contributions of the complete expression of the aerodynamic force are negligible. In case of turbulent boundary layer, the same analysis remarks the importance of a term associated with the turbulent stress tensor. However, it has been shown that this contribution does not need to be computed by a proper choice of the external surface orientation.

The effect of the integration domain has been investigated at different Reynolds numbers and angles of attack. By decomposing the aerodynamic force in surface and volume contributions, it has been possible to identify the specific contributions to the total aerodynamic force.

It has also been numerically verified that as the external boundary of the computational domain tends towards infinity, the lift reduces to the volume integral of the Lamb vector (vortex force), whereas the drag coefficient results expressed by a surface integral intersecting the airfoil wake. For this last case, the accuracy of the drag is sensitive to the solution quality in the flow region where the surface is located.

From a numerical point of view, the most accurate values of the aerodynamic force have been obtained with an integration domain that intersects the wake just downstream the airfoil trailing edge and that contains the whole boundary-layer region. A certain dependency upon the outer boundary conditions has been noted.

The case of an unsteady and turbulent flowfield around an oscillating airfoil has been discussed. A pre stall and a dynamic-stall conditions have been taken into account. The decomposition of the aerodynamic force into the volume and surface contributions has permitted to detect the effects of the free vorticity shed in the wake. In the pre stall case, the effects of the bound vorticity have also been recognized as the contributions in phase with the instantaneous angular position of the airfoil. In the dynamic-stall case, this analysis provides useful information on the dynamic-stall vortex.

The far-field method discussed in the present paper represents an useful device for the analysis of the aerodynamic force. The method can also be applied in unsteady flow solutions with massive separation, provided an accurate numerical simulation is supplied.

The applications carried out demonstrate the reliability of the approach as well as its coherence with other existing theories.

Appendix A: Derivative Moment Transformations

Let Ω be a subset of R^d, where $d = 2, 3$ is the space dimension, having a regular boundary $\partial\Omega$ and $\underline{f}$ a vector field defined in Ω. The following integral relations are applicable (see Wu et al. [17]):

$$\int_\Omega \underline{f}\, \mathrm{d}V = \int_\Omega \underline{\mathbf{r}} \times (\underline{\nabla} \times \underline{f})\, \mathrm{d}V - \int_{\partial\Omega} \underline{\mathbf{r}} \times (\underline{n} \times \underline{f})\, \mathrm{d}S \tag{A1}$$

For a vector field $\phi \underline{n}$, the following identity is also applicable:

$$\int_{\partial\Omega} \phi \underline{n}\, \mathrm{d}S = -\int_{\partial\Omega} \underline{\mathbf{r}} \times (\underline{n} \times \underline{\nabla}\phi)\, \mathrm{d}S \tag{A2}$$

Appendix B: Steady Laminar Boundary-Layer Analysis

The nondimensional form of the equations in case of steady flow (3), (4), and (7) is discussed. U_r and L_r are the velocity and the reference length and $Re_r = U_r L_r/\nu$. We have

$$\underline{\mathbf{F}}^*_{\mathrm{I},d} = -\frac{1}{Re_r}\int_{\Omega^*} (\underline{\mathbf{r}}^* \times \nabla^2 \underline{\omega}^*)\, \mathrm{d}V^* \tag{B1}$$

$$\underline{\mathbf{F}}^*_{\mathrm{II}} = -\frac{1}{Re_r}\int_{\Sigma^*} (\underline{\mathbf{r}}^* \times [\underline{n} \times (\underline{\nabla} \times \underline{\omega}^*)])\, \mathrm{d}S^* + \frac{1}{Re_r}\int_{\Sigma^*} (\underline{\omega}^* \times \underline{n})\, \mathrm{d}S^* \tag{B2}$$

$$\underline{\mathbf{F}}^*_{\mathrm{I},a} = -\int_{\Omega^*} \underline{l}^*\, \mathrm{d}V^* - \int_{\partial\Omega^*} \underline{\mathbf{r}}^* \times (\underline{n} \times \underline{l}^*)\, \mathrm{d}S^* \tag{B3}$$

where * indicates the nondimensional quantities, and $\underline{\mathbf{F}} = U_r^2 L_r^2 \underline{\mathbf{F}}^*$. In case of a two dimensional steady and laminar boundary-layer flow ($Re \gg 1$), the classical analysis of the order of magnitude of the different terms is performed by choosing the correct scaling. Let x and y be the streamwise and the normal wall directions, we introduce $\bar{y} = y/(\delta L_r)$ and $\bar{v} = v/(\delta U_r)$, where $\delta \approx 1/\sqrt{Re}$ is the length scale of the boundary layer [27], and $\underline{\omega} = \omega \underline{k}$. We have that

$$\omega = \frac{\partial v}{\partial y} - \frac{\partial u}{\partial y} = \frac{U_r}{L_r}\left(\delta \frac{\partial \bar{v}}{\partial x^*} - \frac{1}{\delta}\frac{\partial u^*}{\partial \bar{y}}\right) \approx -\frac{U_r}{\delta L_r}\frac{\partial u^*}{\partial \bar{y}}$$

By calculating the integrand functions of Eq. (3) we have

$$\underline{\mathbf{r}} \times \nabla^2 \underline{\omega} = \frac{U_r}{L_r^2}\left(\frac{1}{\delta} x^* \underline{j} - \bar{y}\, \underline{i}\right)\left(\frac{\partial^3 u^*}{\partial x^{*2} \partial \bar{y}} + \frac{1}{\delta^2}\frac{\partial^3 u^*}{\partial \bar{y}^3}\right)$$

Taking into account that $\mathrm{d}V = L_r^3 \delta\, \mathrm{d}V^*$ and $\nu = U_r L_r \delta^2$ we obtain that

$$\nu(\underline{\mathbf{r}} \times \nabla^2 \underline{\omega})\,\mathrm{d}V = L_r^2 U_r^2 (\delta^2 x^* \underline{j} - \delta^3 \bar{y}\,\underline{i}) \left(\frac{\partial^3 u^*}{\partial x^{*2} \partial \bar{y}} + \frac{1}{\delta^2} \frac{\partial^3 u^*}{\partial \bar{y}^3} \right) \mathrm{d}V^*$$

Thus, the component along x direction is given by

$$\underline{\mathbf{F}}^*_{\mathrm{I},d} \cdot \underline{i} = \delta \int_{\Omega^*} \bar{y} \frac{\partial^3 u^*}{\partial \bar{y}^3}\,\mathrm{d}V^* + \mathcal{O}(\delta^3) \tag{B4}$$

and the normal wise component is

$$\underline{\mathbf{F}}^*_{\mathrm{I},d} \cdot \underline{j} = -\int_{\Omega^*} x^* \frac{\partial^3 u^*}{\partial \bar{y}^3}\,\mathrm{d}V^* + \mathcal{O}(\delta^2) \tag{B5}$$

Concerning the advection form integrals expressed by Eq. (7) the same procedure provides

$$\underline{\mathbf{F}}^*_{\mathrm{I},a} \cdot \underline{i} = -\delta \left(\int_{\Omega^*} \bar{v} \frac{\partial u^*}{\partial \bar{y}}\,\mathrm{d}V^* + \int_{\Sigma^*} \bar{y} u^* \frac{\partial u^*}{\partial \bar{y}} n_x\,\mathrm{d}S^* \right) + \mathcal{O}(\delta^2) \tag{B6}$$

$$\underline{\mathbf{F}}^*_{\mathrm{I},a} \cdot \underline{j} = \left(\int_{\Omega^*} u^* \frac{\partial u^*}{\partial \bar{y}}\,\mathrm{d}V^* - \int_{\Sigma^*} x^* u^* \frac{\partial u^*}{\partial \bar{y}} n_x\,\mathrm{d}S^* \right) + \mathcal{O}(\delta) \tag{B7}$$

Finally,

$$\underline{\mathbf{F}}^*_{\mathrm{II}} \cdot \underline{i} = \delta^2 \int_{\Sigma^*} \left(-\frac{\partial^2 u^*}{\partial \bar{y}^2} \bar{y} + \frac{\partial u^*}{\partial \bar{y}} \right) n_y\,\mathrm{d}S^* + \mathcal{O}(\delta^3) \tag{B8}$$

$$\underline{\mathbf{F}}^*_{\mathrm{II}} \cdot \underline{j} = \delta \int_{\Sigma^*} \frac{\partial^2 u^*}{\partial \bar{y}^2} x^* n_y\,\mathrm{d}S^* + \mathcal{O}(\delta^2) \tag{B9}$$

It is worth noting that this contribution is zero on Σ when $n_y = 0$. By resuming, we have obtained that

$$\underline{\mathbf{F}}^*_{\mathrm{I},d} \cdot \underline{i} \approx \mathcal{O}(\delta) \qquad \underline{\mathbf{F}}^*_{\mathrm{I},a} \cdot \underline{i} \approx \mathcal{O}(\delta) \qquad \underline{\mathbf{F}}^*_{\mathrm{II}} \cdot \underline{i} \approx \mathcal{O}(\delta^2)$$

and

$$\underline{\mathbf{F}}^*_{\mathrm{I},d} \cdot \underline{j} \approx \mathcal{O}(1) \qquad \underline{\mathbf{F}}^*_{\mathrm{I},a} \cdot \underline{j} \approx \mathcal{O}(1) \qquad \underline{\mathbf{F}}^*_{\mathrm{II}} \cdot \underline{j} \approx \mathcal{O}(\delta)$$

Appendix C: Steady Turbulent Boundary-Layer Analysis

In case of a turbulent boundary layer on a wall, the previous analysis still holds for the mean flow quantities, by considering $\delta = Re^{-\beta}$, with $\beta > 1/2$. The additional term $\langle \underline{\mathbf{F}}^t \rangle$ in general is not negligible. By expressing the integral (17) in terms of the Reynolds stress tensor, we have

$$\langle \underline{\mathbf{F}}^t \rangle = \int_\Sigma \underline{\mathbf{x}} \times \underline{n} \times (\underline{\nabla} \cdot \underline{\underline{\tau}}^t)\,\mathrm{d}S + \int_\Sigma \underline{\underline{\tau}}^t \cdot \underline{n}\,\mathrm{d}S \tag{C1}$$

In a turbulent boundary layer only the derivatives of the shear stress components τ^t_{xy} have the same order of magnitude of the mean quantities (see Pope [19], p. 114). Thus, within this approximation,

$$[\underline{\mathbf{r}} \times (\underline{n} \times \underline{\nabla} \cdot \underline{\underline{\tau}}^t)]_x \approx -\bar{y} n_y \frac{\partial \tau^t_{xy}}{\partial \bar{y}} \tag{C2}$$

$$[\underline{\mathbf{r}} \times (\underline{n} \times \underline{\nabla} \cdot \underline{\underline{\tau}}^t)]_y \approx x n_y \frac{\partial \tau^t_{xy}}{\partial \bar{y}} \tag{C3}$$

while the terms $\underline{\underline{\tau}}^t \cdot \underline{n}$ results negligible. As a consequence, the integral (C1) reduces to

$$\langle \underline{\mathbf{F}}^t \rangle \approx \int_\Sigma \frac{\partial \tau^t_{xy}}{\partial y} n_y (y\underline{i} - x\underline{j})\,\mathrm{d}S \tag{C4}$$

It is worth noting that this contribution is not negligible, but is zero on Σ when $n_y = 0$.

Appendix D: Some Effects of the Computational Domain

In Fig. D1a a plot of $(C_l)^*_{\Sigma_I}$ is shown obtained by moving the outer boundary at a distance $y_S \sim 50c$. It is visible a marked reduction in the slope with respect to the case $y_S = 15c$. In Fig. D1b, the term $(C_l)^*_{\Sigma_J}$ reveals the presence of vorticity diffused upstream the airfoil. As the distance y_S of the external boundary from the body increases, the contribution $(C_l)^*_{\Sigma_J}$ vanishes.

Appendix E: Self-Similar Solution of Turbulent Wakes

A self-similar solution occurs in the turbulent wakes downstream of no lifting bodies (see [19], p. 147). By defining $\langle u \rangle = U_\infty - u_s(x) f(\xi)$, where $\xi = y/y_{1/2}(x)$, is the similar variable, and $y_{1/2}(x)$ is the wake width:

$$\langle u(x, \pm y_{1/2}(x)) \rangle = U_\infty - \frac{1}{2} u_s(x) \tag{E1}$$

and $u_s(x) = U_\infty - \langle u(x, 0) \rangle$, in the hypothesis of a constant turbulent viscosity, the normalized velocity defect $f(\xi)$ is obtained analytically as

$$f(\xi) = e^{-\beta \xi^2} \tag{E2}$$

where $\beta \approx 0.693$.

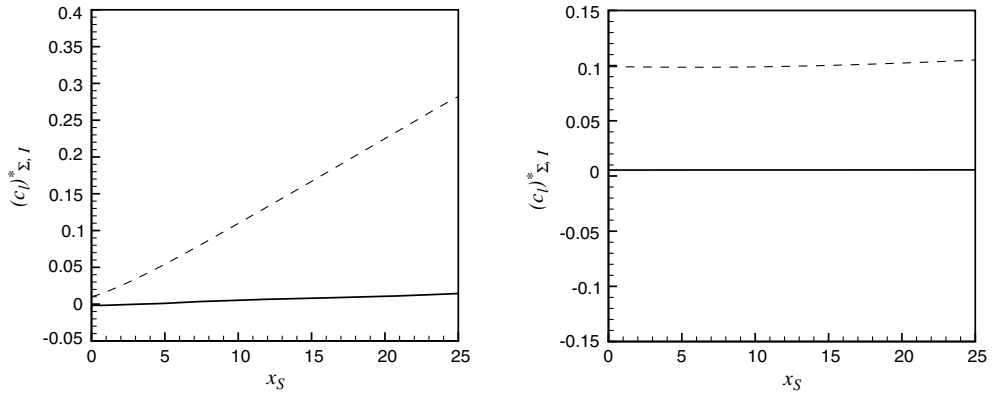

a) b)

Fig. D1 NACA0012 airfoil, turbulent flow solutions at $Re = 1.0 \times 10^7$ and angle of attack $\alpha = 6°$. Normalized contributions of lift coefficients by varying the outer boundary distance. Solid line, $y_S = 50c$; and dotted line, $y_S = 15c$: a) $(C_l)^*_{\Sigma_I}$ and b) $(C_l)^*_{\Sigma_J}$.

References

[1] Laflin, K. R., Klausmeyer, S. M., Zickuhr, T., Vassberg, J. C., Wahls, R. A., Morrison, J. H., Brodersen, O. P., Rakowitz, M. E., Tinoco, E. N., and Godard, J. L., "Data Summary from Second AIAA Computational Fluid Dynamics Drag Prediction Workshop," *Journal of Aircraft*, Vol. 42, No. 5, 2005, pp. 1165–1178. doi:10.2514/1.10771

[2] Vassberg, J. C., Tinoco, E., Mani, M., Brodersen, O. P., Eisfeld, B., Wahls, R., Morrison, J., Zickuhr, T., Laflin, K., and Mavriplis, D., "Abridged Summary of the Third AIAA Computational Fluid Dynamics Drag Prediction Workshop," *Journal of Aircraft*, Vol. 45, No. 3, 2008, pp. 781–798. doi:10.2514/1.30572

[3] van Dam, C. P., "Recent Experience with Different Methods of Drag Prediction," *Progress in Aerospace Sciences*, Vol. 35, No. 8, 1999, pp. 751–798. doi:10.1016/S0376-0421(99)00009-3

[4] Yamazaki, W., Matsushima, K., and Nakahashi, K., "Aerodynamic Design Optimization Using the Drag-Decomposition Method," *AIAA Journal*, Vol. 46, No. 5, 2008, pp. 1096–1106. doi:10.2514/1.30342

[5] Tognaccini, R., "Methods for Drag Decomposition, Thrust-Drag Bookkeeping from CFD Calculations," *CFD-Based Aircraft Drag Prediction and Reduction*, von Karman Inst. for Fluid Dynamics Lecture Series, Rhode St-Genese, Belgium, 2003.

[6] Destarac, D., and van der Vooren, J., "Drag-Thrust Analysis of Jet-Propelled Transonic Transport Aircraft, Definition of Physical Drag Components," *Aerospace Science and Technology*, Vol. 8, No. 6, 2004, pp. 545–556. doi:10.1016/j.ast.2004.03.004

[7] Spalart, P. R., "On the Far Wake and Induced Drag of Aircraft," *Journal of Fluid Mechanics*, Vol. 603, May 2008, pp. 413–430. doi:10.1017/S0022112008001146

[8] Kurtulus, D. F., Scarano, F., and David, L., "Unsteady Aerodynamic Forces Estimation on a Square Cylinder by TR-PIV," *Experiments in Fluids*, Vol. 42, No. 2, Feb. 2007, pp. 185–196. doi:10.1007/s00348-006-0228-4

[9] Ferreira, C. S., van Bussel, G., Scarano, F., and van Kuik, G., "PIV Visualization of Dynamic Stall VAWT and Blade Load Determination," 46th AIAA Aerospace Sciences Meeting and Exhibit, AIAA Paper 2008-1317, Reno, NV, 7–10 Jan. 2008.

[10] Paparone, L., and Tognaccini, R., "Computational Fluid Dynamics-Based Drag Prediction and Decomposition," *AIAA Journal*, Vol. 41, No. 9, 2003, pp. 1647–1657. doi:10.2514/2.7300

[11] Tognaccini, R., "Drag Computation and Breakdown in Power-On Conditions," *Journal of Aircraft*, Vol. 42, No. 1, 2005, pp. 245–252. doi:10.2514/1.8510

[12] von Karman, T., and Burgers, J. M., "General Aerodynamic Theory-Perfect Fluids," *Aerodynamic Theory*, edited by W. F. Durand, Vol. 2, Springer, Berlin, 1935.

[13] Saffman, P. G., *Vortex Dynamics*, Cambridge Univ. Press, Cambridge, England, U.K., 1992.

[14] Wu, J. C., "Theory for Aerodynamic Force and Moment in Viscous Flows," *AIAA Journal*, Vol. 19, No. 4, 1981, pp. 432–441. doi:10.2514/3.50966

[15] Panda, J., and Zaman, K. B. M. Q., "Experimental Investigation of the Flowfield of an Oscillating Airfoil and Estimation of Lift from Wake Surveys," *Journal of Fluid Mechanics*, Vol. 265, 1994, pp. 65–95. doi:10.1017/S0022112094000765

[16] Noca, F., Shiels, D., and Jeon, D., "A Comparison of Methods for Evaluating Time-Dependent Fluid Dynamic Forces on Bodies, Using only Velocity Fields and Their Derivatives," *Journal of Fluids and Structures*, Vol. 13, No. 5, 1999, pp. 551–578. doi:10.1006/jfls.1999.0219

[17] Wu, J.-Z., Ma, H.-Y., and Zhou, M.-D., *Vorticity and Vortex Dynamics*, Springer, New York, 2006.

[18] Wu, J.-Z., Lu, X.-Y., and Zhuang, L.-X., "Integral Force Acting on a Body due to Local Flow Structures," *Journal of Fluid Mechanics*, Vol. 576, 2007, pp. 265–286. doi:10.1017/S0022112006004551

[19] Pope, S. B., *Turbulent Flows*, Cambridge Univ. Press, Cambridge, England, U.K., 2000.

[20] Wu, J. Z., Zhou, Y., Lu, X. Y., and Fan, M., "Turbulence Force as a Diffusive Field with Vortical Sources," *Physics of Fluids*, Vol. 11, No. 3, 1999, pp. 627–635. doi:10.1063/1.869934

[21] Jameson, A., Schmidt, W., and Turkel, E., "Numerical Solutions of the Euler Equations by Finite Volume Methods Using Runge–Kutta Time Stepping Schemes," 14th Fluid and Plasma Dynamics Conference, AIAA Paper 1981-1259, Palo Alto, CA, 23–25 June 1981, p. 15.

[22] Kok, J., "Resolving the Dependence on Free-Stream Values for the κ-ω Turbulence Model," *AIAA Journal*, Vol. 38, No. 7, 2000, pp. 1292–1295. doi:10.2514/2.1101

[23] Menter, F. R., "Two Equation Eddy Viscosity Turbulence Models for Engineering Applications," *AIAA Journal*, Vol. 32, No. 8, 1994, pp. 1598–1605. doi:10.2514/3.12149

[24] McCroskey, W. J., "A Critical Assessment of Wind Tunnel Results for the NACA0012 Airfoil," NASA TM-100019, Oct. 1987.

[25] Betz, A., "A Method for the Direct Determination of Wing-Section Drag," *Zeitschrift für Flugtechnik und Motorluftschiffahrt*, Vol. 6, 1925.

[26] Lee, T., and Gerontakos, P., "Investigation of Flow over an Oscillating Airfoil," *Journal of Fluid Mechanics*, Vol. 512, 2004, pp. 313–341. doi:10.1017/S0022112004009851

[27] Schlichting, H., and Gersten, K., *Boundary-Layer Theory*, 8th ed., Springer–Verlag, Berlin, 1999.

A. Tumin
Associate Editor